Fast method to compute scattering by a buried object under a randomly rough surface: PILE combined with FB-SA

Christophe Bourlier,* Gildas Kubické, and Nicolas Déchamps

IREENA (Institut de Recherche en Electrotechnique et Electronique de Nantes Atlantique), Radar Team, Polytech'Nantes, Rue Christian Pauc, La Chantrerie, BP 50609, 44306 Nantes Cedex 3, France
**Corresponding author: christophe.bourlier@univ-nantes.fr*

Received October 25, 2007; accepted January 24, 2008;
posted February 4, 2008 (Doc. ID 89029); published March 19, 2008

A fast, exact numerical method based on the method of moments (MM) is developed to calculate the scattering from an object below a randomly rough surface. Déchamps *et al.* [J. Opt. Soc. Am. A **23**, 359 (2006)] have recently developed the PILE (propagation-inside-layer expansion) method for a stack of two one-dimensional rough interfaces separating homogeneous media. From the inversion of the impedance matrix by block (in which two impedance matrices of each interface and two coupling matrices are involved), this method allows one to calculate separately and exactly the multiple-scattering contributions inside the layer in which the inverses of the impedance matrices of each interface are involved. Our purpose here is to apply this method for an object below a rough surface. In addition, to invert a matrix of large size, the forward-backward spectral acceleration (FB-SA) approach of complexity $\mathcal{O}(N)$ (N is the number of unknowns on the interface) proposed by Chou and Johnson [Radio Sci. **33**, 1277 (1998)] is applied. The new method, PILE combined with FB-SA, is tested on perfectly conducting circular and elliptic cylinders located below a dielectric rough interface obeying a Gaussian process with Gaussian and exponential height autocorrelation functions. © 2008 Optical Society of America

OCIS codes: 290.5880, 290.4210, 280.0280.

1. INTRODUCTION

The study of scattering from an object located below a rough surface is a subject of great interest. The applications of such research include detection of land mines, pipes, and other buried objects. When the surface is smooth and the buried object is an infinite cylinder, and by using a decomposition of the scattered fields as a sum of cylindrical eigenfunctions, the problem can be solved analytically [1–3] by the introduction of Bessel functions. For an object near a slightly rough surface, some asymptotic models can be found [4–9]. Exact numerical methods based on the extinction theorem combined with the method of moments (MM) [10] have also been developed for two-dimensional [11–17] and three-dimensional [18–20] problems.

In numerical simulation of the scattering from a buried object, the length of the surface plays an important role: It has to be large enough for the scattered field to vanish at the surface extremities, that is, to avoid edge effects. Thus, it is interesting to investigate exact, fast numerical methods to treat a large problem. Such methods have been developed for a single rough surface. For instance, one can cite the banded-matrix-iterative-approach/canonical grid (BMIA-CAG) of Tsang *et al.* [21,22] of complexity $\mathcal{O}(N \log N)$, the forward-backward (FB) method of Holliday *et al.* [23] of complexity $\mathcal{O}(N^2)$, and the accelerated version forward-backward spectral acceleration (FB-SA) of Chou and Johnson [24] and Torrungrueng *et al.* [25] of complexity $\mathcal{O}(N)$, in which in all cases N is the number of samples on the surface.

Recently, Déchamps *et al.* [26] have developed a fast numerical method, propagation-inside-layer expansion (PILE), devoted to the scattering by a stack of two one-dimensional interfaces separating homogeneous media. The main advantage of the PILE method is that the resolution of the linear system (obtained by the method of moments) is broken down into different steps: (1) two steps dedicated to solving for the local interactions, which can be done by efficient methods valid for a single rough interface, such as FB-SA and BMIA/-CAG, and (2) two dedicated to solving for the coupling interactions, which can be done by updating the previous efficient methods. The latter has been recently investigated with BMIA-CAG [27] and FB-SA [28].

In this paper, the PILE method is applied to an object located below a rough surface. In addition, to accelerate PILE and to treat large problems, the local interactions on the upper surface are computed by FB-SA. Since the number of unknowns on the surface is much greater than on the object, the complexity of the method is then $\mathcal{O}(N)$.

This paper is organized as follows. In Section 2, PILE combined with FB-SA for the calculation of the local interactions on the upper dielectric rough interface is presented. In Section 3, the convergence of the accelerated PILE method is investigated for perfectly conducting circular and elliptic cylinders located below a rough surface. Section 4 presents our conclusions.

 © 2008 Optical Society of America

2. PILE METHOD

A. Geometry of the Problem

As shown in Fig. 1, we consider an object Σ_- of equation z_- buried below a rough surface Σ_+ of equation z_+. The problem is assumed to be two-dimensional (invariant along $\hat{\mathbf{y}}$), and the incident vector lies in the $(\hat{\mathbf{x}},\hat{\mathbf{z}})$ plane. z_+ is assumed to be a Gaussian stationary stochastic process with zero mean value ($\langle z_+\rangle=0$). The surface height spectrum can be of any kind. z_- is a deterministic function defined with respect to its center $\{x_c,-h_c\}$ with $h_c>0$ (depth). One must pay special attention to avoid any intersection between z_+ and z_-.

The random surface Σ_+ can easily be generated by a spectral method widely used in the calculation of wave scattering [10]. If N_+ represents the number of samples, the discretized abscissa and heights of the rough surface are given by $x_+^n=-L_+/2+(n-1/2)\Delta x_+$ and $z_+^n=z_+(x_+^n)$, respectively, with $n\in[1;N_+]$. $\Delta x_+=L_+/N_+$ is the sampling step and L_+ the length of the surface. In the same manner, one defines for the object $z_-^m=z_-(x_-^m)$ with $m\in[1;N_-]$, where N_- is the number of samples. According to the object shape, z_- must be a bijective function. For example for an elliptic cylinder of major and minor semiaxis $\{a,b\}$, the polar coordinates $(a,b,\phi\in[0;2\pi])$ are used to express a point location on the cylinder. This leads to $\{x_-=x_c+a\cos\phi, z_-=-h_c+b\sin\phi\}$. For a circular cylinder $a=b$, where a is the radius. A point of the plane $(\hat{\mathbf{x}},\hat{\mathbf{z}})$ will be denoted by $\mathbf{r}=x\hat{\mathbf{x}}+z\hat{\mathbf{z}}$ and a point belonging to $\Sigma_\pm$ by $\mathbf{r}_\pm=x_\pm\hat{\mathbf{x}}+z_\pm\hat{\mathbf{z}}$. The random interface is separated by two nonmagnetic, semi-infinite, homogeneous media $\Omega_{1,2}$ of relative permittivity $\epsilon_{r1,r2}$, and the relative permittivity of the nonmagnetic object is ϵ_{r3}.

To avoid edge limitations, the incident field ψ_i is chosen as a Thorsos' tapered plane wave [29] defined as

$$\psi_i(\mathbf{r})=\exp(j\mathbf{k}_i\cdot\mathbf{r})\exp\left(-\frac{(x+z\tan\theta_i)^2}{g^2}\right)\exp[jw(\mathbf{r})\mathbf{k}_i\cdot\mathbf{r}], \tag{1}$$

in which $w(\mathbf{r})=[2(x+z\tan\theta_i)^2/g^2-1]/(K_1g\cos\theta_i)^2$, and $\mathbf{k}_i=K_1(\hat{\mathbf{x}}\sin\theta_i-\hat{\mathbf{z}}\cos\theta_i)$ is the incident wave vector. θ_i is the incident angle defined with respect to $\hat{\mathbf{z}}$ in the counterclockwise direction (Fig. 1), K_1 is the wave number in the incident medium Ω_1, and g stands for the tapering parameter, which has a dimension of length (controls the spatial extent of the incident wave). Since the paper is devoted to moderate incidence angles, this wave is appropriate and satisfies Maxwell's equations with good accuracy. An $e^{-j\omega t}$ time-harmonic convention is used. Furthermore, the TE (electric field along $\hat{\mathbf{y}}$ direction) and TM (magnetic field along $\hat{\mathbf{y}}$ direction) polarizations are considered.

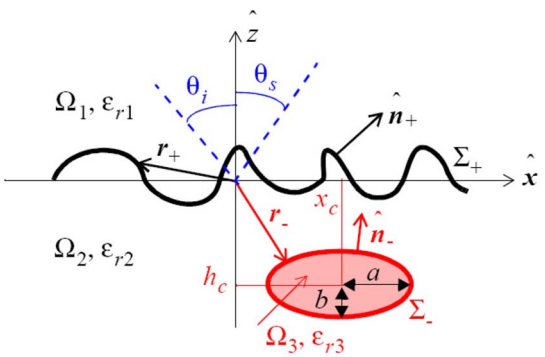

Fig. 1. (Color online) Geometry of the problem.

B. PILE Description

This new method has been recently developed by Déchamps *et al.* in [26] and was thoroughly studied there. The main equations are given below.

Using the extinction theorem both on the rough interface and object and on the boundary conditions, we obtain four coupled integral equations (see, for instance, [14,15,26–28]). It is important to note that the integral equations for an object located below a rough surface or for a stack of two rough interfaces are the same.

The use of the MM with point matching and pulse basis functions leads to the linear system

$$\bar{\mathbf{Z}}\mathbf{X}=\mathbf{s}, \tag{2}$$

where $\bar{\mathbf{Z}}$ (the overbar stands for a matrix) is the impedance matrix of size $2(N_++N_-)\times2(N_++N_-)$. The unknown vector $\mathbf{X}$ of length $2(N_++N_-)$ is equal to

$$\mathbf{X}^{\mathrm{T}}=[\mathbf{X}_+^{\mathrm{T}}\quad\mathbf{X}_-^{\mathrm{T}}], \tag{3}$$

where superscript T stands for the transpose operator. $\mathbf{X}_\pm$ of length $2N_\pm$ contains the unknown fields $\psi_\pm$ and their normal derivatives $\partial\psi_\pm/\partial n_\pm$ on the upper surface and on the object, so that

$$\mathbf{X}_\pm^{\mathrm{T}}=\left[\underbrace{\psi(r_\pm^1)\ldots\psi(r_\pm^{N_\pm})}_{N_\pm\text{times}}\underbrace{\frac{\partial\psi(r_\pm^1)}{\partial n_\pm}\ldots\frac{\partial\psi(r_\pm^{N_\pm})}{\partial n_\pm}}_{N_\pm\text{times}}\right]. \tag{4}$$

The source term $\mathbf{s}$ is defined as

$$\mathbf{s}^{\mathrm{T}}=[\mathbf{s}_+^{\mathrm{T}}\quad\mathbf{s}_-^{\mathrm{T}}]=[\mathbf{s}_+^{\mathrm{T}}\quad\mathbf{0}^{\mathrm{T}}], \tag{5}$$

with

$$\mathbf{s}_+^{\mathrm{T}}=\left[\underbrace{\psi_i(r_+^1)\ldots\psi_i(r_+^{N^+})}_{N_+\text{times}}\underbrace{0\ldots0}_{N_+\text{times}}\right], \tag{6}$$

and $\mathbf{s}_-=\mathbf{0}$, because the incident field illuminates only the upper surface.

To solve efficiently the linear system (2), the impedance matrix $\bar{\mathbf{Z}}$ is expressed from submatrices [26] as

$$\bar{\mathbf{Z}}=\begin{bmatrix}\bar{\mathbf{Z}}_+ & \bar{\mathbf{Z}}_\mp\\ \bar{\mathbf{Z}}_\pm & \bar{\mathbf{Z}}_-\end{bmatrix}. \tag{7}$$

$\{\bar{\mathbf{Z}}_\pm\}$ correspond exactly to the impedance matrices [size $(2N_\pm)\times(2N_\pm)$] of $\Sigma_\pm$. Matrices $\bar{\mathbf{Z}}_\mp$ [size $(2N_+)\times(2N_-)$] and $\bar{\mathbf{Z}}_\pm$ [size $(2N_-)\times(2N_+)$] can be interpreted as coupling matrices between Σ_+ and Σ_-. The complete expression of these matrices can be found in Appendix A.

First, the scattered field on the upper surface $\mathbf{X}_+$ is derived. It is approximated as follows [26]:

$$\mathbf{X}_+ = \left[\sum_{p=0}^{p=P_{\mathrm{PILE}}} \bar{\mathbf{M}}_c^p\right] \bar{\mathbf{Z}}_+^{-1}\mathbf{s}_+ = \sum_{p=0}^{p=P_{\mathrm{PILE}}} \mathbf{Y}_+^{(p)}, \tag{8}$$

in which

$$\begin{cases} \mathbf{Y}_+^{(0)} = \bar{\mathbf{Z}}_+^{-1}\mathbf{s}_+ & \text{for } p=0 \\ \mathbf{Y}_+^{(p)} = \bar{\mathbf{M}}_c\mathbf{Y}_+^{(p-1)} & \text{for } p>0 \end{cases}, \tag{9}$$

and $\bar{\mathbf{M}}_c$ is the characteristic matrix of the "surface +object" defined as

$$\bar{\mathbf{M}}_c = \bar{\mathbf{Z}}_+^{-1}\bar{\mathbf{Z}}_{\mp}\bar{\mathbf{Z}}_-^{-1}\bar{\mathbf{Z}}_{\pm}. \tag{10}$$

In addition, the scattered field on the object $\mathbf{X}_-$ is expressed from $\mathbf{X}_+$ as

$$\mathbf{X}_- = -\bar{\mathbf{Z}}_-^{-1}\bar{\mathbf{Z}}_{\pm}\mathbf{X}_+. \tag{11}$$

We define the norm $|\bar{\mathbf{M}}_c|$ of a complex matrix by its spectral radius, i.e., the modulus of its eingenvalue that has the highest modulus. Expansion (9) is then valid if $|\bar{\mathbf{M}}_c|$ is strictly smaller than one. The physical interpretation of $\bar{\mathbf{M}}_c$ is shown in Fig. 2 of [26]: In the zeroth order term, $\bar{\mathbf{Z}}_+^{-1}$ accounts for the local interactions on the upper surface, so $\mathbf{Y}_+^{(0)}$ corresponds to the contribution of the direct scattering on the upper surface, without interaction with the object; in the first-order term, $\mathbf{Y}_+^{(1)}=\bar{\mathbf{M}}_c\mathbf{Y}_+^{(0)}$, $\bar{\mathbf{Z}}_{\pm}$ propagates the resulting upper field information $\mathbf{Y}_+^{(0)}$ toward the lower interface (the buried object), $\bar{\mathbf{Z}}_-^{-1}$accounts for the local interactions on this object, and $\bar{\mathbf{Z}}_{\mp}$ repropagates the resulting contribution toward the upper interface; finally, $\bar{\mathbf{Z}}_+^{-1}$ updates the field values on the upper interface. In conclusion, the order P_{PILE} of PILE corresponds to the P_{PILE} reflections between the surface and the object.

If the object dimension is of the order of the wavelength and if Δx_+ is of the order of Δx_-, then the number of samples on the surface Σ_+ is much greater than that of the object Σ_-, $N_+ \gg N_-$. Thus, the most complex operation in the calculation of $\bar{\mathbf{M}}_c$ is $\bar{\mathbf{Z}}_+^{-1}\mathbf{Y}$. One of the advantages of the PILE method is the ability to apply fast exact methods that already exist for a single rough surface, like for instance the BMIA-CAG of Tsang *et al.* [21,22] of complexity $\mathcal{O}(N_+ \log N_+)$, the FB method of Holliday *et al.* [23] of complexity $\mathcal{O}(N_+^2)$, and the accelerated version of FB-SA of Chou and Johnson [24] and Torrungrueng *et al.* [25] of complexity $\mathcal{O}(N_+)$. The purpose of this paper is to implement PILE combined with the FB-SA algorithm for a buried object.

C. Forward-Backward Method

In this subsection, the FB method is applied to speed up the calculation of $\bar{\mathbf{Z}}_+^{-1}\mathbf{u}$ ($\mathbf{u}$ is the column vector of length $2N_+$) to reduce the complexity to $\mathcal{O}(N_+^2)$ instead of the $\mathcal{O}(N_+^3)$ from a direct lower upper (LU) inversion. For a perfectly conducting surface, this method was developed by Holliday [23] *et al.* and more recently, it has been extended to a dielectric surface by Iodice [30]. In what follows, the main equations are given in order to explain the acceleration SA.

We want to solve $\bar{\mathbf{Z}}_+\mathbf{u}=\mathbf{v} \Leftrightarrow \mathbf{u}=\bar{\mathbf{Z}}_+^{-1}\mathbf{v}$, where $\mathbf{u}$ (the unknown) and $\mathbf{v}$ are column vectors of length $2N_+$. From Eq. (A1), the $\bar{\mathbf{Z}}_+$ matrix is expressed from four square submatrices of sizes $N_+ \times N_+$ as

$$\bar{\mathbf{Z}}_+ = \begin{bmatrix} \bar{\mathbf{A}} & \bar{\mathbf{B}} \\ \bar{\mathbf{C}} & \bar{\mathbf{D}} \end{bmatrix}, \tag{12}$$

in which $\bar{\mathbf{A}}=\bar{\mathbf{A}}_+$, $\bar{\mathbf{B}}=\bar{\mathbf{B}}_+$, $\bar{\mathbf{C}}=\bar{\mathbf{C}}_+$, and $\bar{\mathbf{D}}=\rho_{21}\bar{\mathbf{D}}_+$. The FB algorithm decomposes $\bar{\mathbf{Z}}_+\mathbf{u}=\mathbf{v}$ as

$$\begin{cases} \bar{\mathbf{A}}_d\mathbf{u}_{1f} + \bar{\mathbf{B}}_d\mathbf{u}_{2f} = \mathbf{v}_1 - \bar{\mathbf{A}}_f\mathbf{u}_1 - \bar{\mathbf{B}}_f\mathbf{u}_2 \\ \bar{\mathbf{C}}_d\mathbf{u}_{1f} + \bar{\mathbf{D}}_d\mathbf{u}_{2f} = \mathbf{v}_2 - \bar{\mathbf{C}}_f\mathbf{u}_1 - \bar{\mathbf{D}}_f\mathbf{u}_2 \end{cases}, \tag{13}$$

and

$$\begin{cases} \bar{\mathbf{A}}_d\mathbf{u}_{1b} + \bar{\mathbf{B}}_d\mathbf{u}_{2b} = -\bar{\mathbf{A}}_b\mathbf{u}_1 - \bar{\mathbf{B}}_b\mathbf{u}_2 \\ \bar{\mathbf{C}}_d\mathbf{u}_{1b} + \bar{\mathbf{D}}_d\mathbf{u}_{2b} = -\bar{\mathbf{C}}_b\mathbf{u}_1 - \bar{\mathbf{D}}_b\mathbf{u}_2 \end{cases}. \tag{14}$$

For instance, $\bar{\mathbf{A}}_d$ is a *diagonal* matrix, $\bar{\mathbf{A}}_f$ a *lower* triangular matrix, and $\bar{\mathbf{A}}_b$ an *upper* triangular matrix, all built from $\bar{\mathbf{A}}$ ($\bar{\mathbf{A}}=\bar{\mathbf{A}}_f+\bar{\mathbf{A}}_d+\bar{\mathbf{A}}_b$). The subscripts $\{d,f,b\}$ stand for diagonal, forward, and backward matrices but are referred to, respectively, as diagonal, lower, and upper triangular matrices. Moreover, $\mathbf{u}^{\mathrm{T}}=[\mathbf{u}_1^{\mathrm{T}} \ \mathbf{u}_2^{\mathrm{T}}]$ and $\mathbf{v}^{\mathrm{T}}=[\mathbf{v}_1^{\mathrm{T}} \ \mathbf{v}_2^{\mathrm{T}}]$, in which $\{\mathbf{u}_1,\mathbf{u}_2,\mathbf{v}_1,\mathbf{v}_2\}$ are column vectors of length N_+. Finally, the unknown vectors are decomposed as $\mathbf{u}_i=\mathbf{u}_{if}+\mathbf{u}_{ib}$ ($i=\{1,2\}$), in which $\mathbf{u}_{if}$ gives the *forward* contribution (from the points on the *left* of the current point) and $\mathbf{u}_{ib}$ gives the *backward* contribution (from the *right*). The surface is oriented by assuming that the incident beam propagates from left to right.

To compute $\mathbf{u}$, an iterative procedure is applied. Assuming first that $\mathbf{u}_b=\mathbf{0} \Rightarrow \mathbf{u}=\mathbf{u}_f+\mathbf{u}_b=\mathbf{u}_f \Rightarrow \mathbf{u}_i=\mathbf{u}_{if}$, Eq. (13) is solved for $\mathbf{u}_f=\mathbf{u}_{1f}+\mathbf{u}_{2f}$. Then, introducing $\mathbf{u}_f$ in Eq. (14), $\mathbf{u}_b$ is found. The first iteration $\mathbf{u}^{(0)}$ is then equal to $\mathbf{u}_f+\mathbf{u}_b$. The scheme is repeated to calculate the next iterations $\mathbf{u}^{(p)}$ up to the order $p=P_{\mathrm{FB}}$. Equations (13) and (14) are very convenient to solve by substitution for $\mathbf{u}_f$ and $\mathbf{u}_b$. For instance, from Eq. (13), since $\{\bar{\mathbf{A}}_f,\bar{\mathbf{B}}_f,\bar{\mathbf{C}}_f,\bar{\mathbf{D}}_f\}$ are lower triangular matrices with null diagonal coefficients, we get, with $m \in [2;N_+]$

$$\begin{cases} A_d^{m,m}u_{1f}^m + B_d^{m,m}u_{2f}^m = v_1^m - \sum_{n=1}^{n=m-1}\left(A_f^{m,n}u_1^n + B_f^{m,n}u_2^n\right) \\ C_d^{m,m}u_{1f}^m + D_d^{m,m}u_{2f}^m = v_2^m - \sum_{n=1}^{n=m-1}\left(C_f^{m,n}u_1^n + D_f^{m,n}u_2^n\right) \end{cases}. \tag{15}$$

For instance, $A^{m,n}$ is the element of the matrix $\bar{\mathbf{A}}$ for the column m and the row n. u_i^n is the nth component of the vector $\mathbf{u}_i$. Thus, assuming first that $\mathbf{u}_b=\mathbf{0} \Rightarrow \mathbf{u}=\mathbf{u}_f+\mathbf{u}_b=\mathbf{u}_f \Rightarrow \mathbf{u}_i=\mathbf{u}_{if}$ and by solving Eq. (15), the unknowns $\{u_{1f}^m,u_{2f}^m\}$ with $m \in [2;N_+]$ are calculated from $4N_+^2/2$ multiplications. From Eq. (14), we obtain an equation system similar to Eq. (15), but the sum over n is $n \in [m+1;N_+]$, and the unknowns $\{u_{1b}^m,u_{1b}^m\}$ with $m \in [1;N_+-1]$ are also calculated from $4N_+^2/2$ multiplications. In conclusion, the complexity of the FB method is $\mathcal{O}(N_+^2)$. By combining the

SA approach, only $\mathcal{O}(N_+)$ multiplications are needed. In Subsection 2.D, the basic concept of the SA is recalled. A more detailed theory can be found in [24,25].

D. FB-SA Method

Let us consider two points $(\mathbf{r}_+^m,\mathbf{r}_+^n)$ belonging to the upper surface Σ_+, and let us denote $x_d=x_+^m-x_+^n$ and $z_d=z_+^m-z_+^n$. $\mathbf{r}_m$ is the observation point, fixed, and $\mathbf{r}_n$ the source point that moves on the surface. The impedance matrix $\bar{\mathbf{Z}}_+$ is given by Eq. (A1). It is expressed from four submatrices, two $\{\bar{\mathbf{A}}_+=\bar{\mathbf{A}},\bar{\mathbf{C}}_+=\bar{\mathbf{C}}\}$ corresponding to the Neumann boundary condition (perfectly conducting surface for the TM polarization), and two $\{\bar{\mathbf{B}}_+=\bar{\mathbf{B}},\bar{\mathbf{D}}_+=\bar{\mathbf{D}}/\rho_{21}\}$ corresponding to the Dirichlet boundary condition (perfectly conducting surface for the TE polarization). Thus, in Eq. (15), the SA algorithm used to speed up the products $A_f^{m,n}u_1^n$ and $C_f^{m,n}u_1^n$ is the same (TM case). The same remark holds for the products $B_f^{m,n}u_2^n$ and $D_f^{m,n}u_2^n$ (TE case).

1. TE Case

From Eq. (A4), the elements of the matrix $\bar{\mathbf{B}}=\bar{\mathbf{B}}_+$ are expressed from the 2D Green function as $B^{m,n}=\Delta x_+ g_1(\mathbf{r}_+^m,\mathbf{r}_+^n)=j\Delta x_+/4H_0^{(1)}(K_1\|\mathbf{r}_+^n-\mathbf{r}_+^m\|)$, in which $H_0^{(1)}$ is the Hankel function of the first kind and zero order. The coefficient α_+^n is included in u_2^n.

Let x_{d0} be the horizontal distance separating the weak interactions from the strong ones, and let N_s be the integer part of $x_{d0}/\Delta x_+$. Then, considering first the *forward* case, the term $\Sigma_{n=1}^{n=m-1}B_f^{m,n}u_2^n$ in Eq. (15) can be written as

$$\sum_{n=1}^{n=m-1} B_f^{m,n}u_2^n = \underbrace{\sum_{n=1}^{n=m-N_s-1} B_f^{m,n}u_2^n}_{E_f^{m,(\mathrm{s})}} + \underbrace{\sum_{n=m-N_s}^{n=m-1} B_f^{m,n}u_2^n}_{E_f^{m,(\mathrm{w})}}. \tag{16}$$

In the above decomposition the term $E_f^{m,(\mathrm{s})}$ is performed exactly for each $m\le N_s+1$, whereas $E_f^{m,(\mathrm{w})}$ is calculated using the SA. The SA is based on the following decomposition of the Green function, written here for $x_m-x_n>0$ [24,25]:

$$g_1(\mathbf{r}_+^m,\mathbf{r}_+^n)=\frac{j}{4\pi}\int_{C_g}\exp\{jK_1[(x_+^m-x_+^n)\cos\phi + (z_+^m-z_+^n)\sin\phi]\}\mathrm{d}\phi, \tag{17}$$

where the integration contour C_g (top of Fig. 2) is defined as $[-\pi/2+j\infty;-\pi/2[\cup[-\pi/2;+\pi/2]\cup]+\pi/2;+\pi/2-j\infty]$. The purpose of SA is to substitute for the path C_g a new path C_δ, which permits us to calculate the numerical integration over ϕ with few angles. The detailed description of this path will be discussed below. Thus $E_f^{m,(\mathrm{s})}$ can be written as

$$\begin{aligned}E_f^{m,(\mathrm{s})}&=\frac{j\Delta x_+}{4\pi}\sum_{n=1}^{m-N_s-1}u_2^n\int_{C_\delta}\exp\{jK_1[(x_+^m-x_+^n)\cos\phi + (z_+^m-z_+^n)\sin\phi]\}\mathrm{d}\phi\\&=\frac{j\Delta x_+}{4\pi}\int_{C_\delta}F_m(\phi)\exp(jK_1z_+^m\sin\phi)\mathrm{d}\phi=\frac{j\Delta x_+}{4\pi}\end{aligned}$$

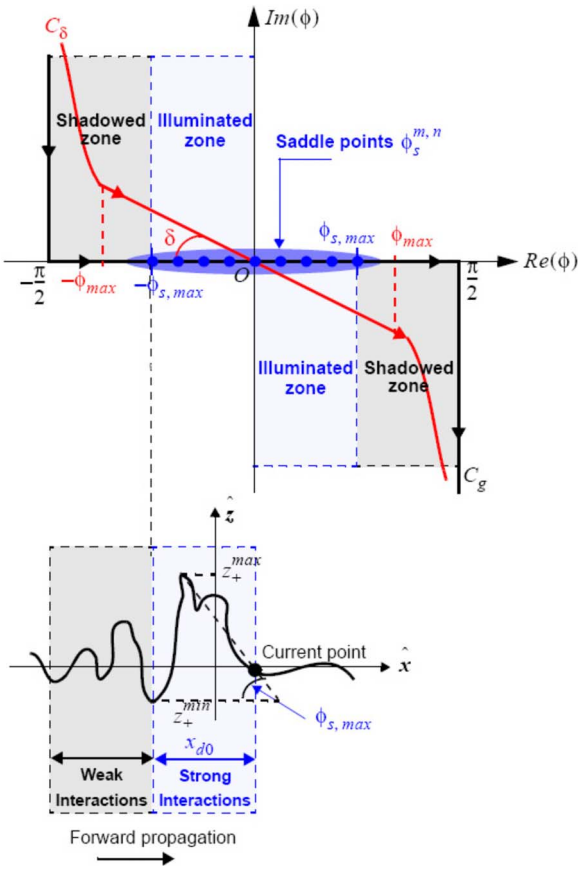

Fig. 2. (Color online) Top, illustration of the integration contours of the 2D Green function C_g, and of that used for the SA algorithm C_δ. Bottom, physical interpretation of C_δ in the spatial domain.

$$\times\exp(-j\delta)\sum_{p=-Q}^{p=+Q}F_m(\phi_p)\exp(jK_1z_+^m\sin\phi_p)\Delta\phi \tag{18}$$

with

$$F_m(\phi)=\sum_{n=1}^{m-N_s-1}u_2^n\exp\{jK_1[(x_+^m-x_+^n)\cos\phi-z_+^n\sin\phi]\}. \tag{19}$$

In addition, $F_m(\phi)$ can be calculated from $F_{m-1}(\phi)$ as

$$\begin{aligned}F_m(\phi)&=F_{m-1}(\phi)\exp(jK_1\Delta x_+\cos\phi)+u_2^{m-N_s-1}\\&\quad\times\exp\{jK_1[(N_s+1)\Delta x_+\cos\phi-z_+^{m-N_s-1}\sin\phi]\}.\end{aligned} \tag{20}$$

When computing the forward steps in Eq. (15), the sum is performed exactly for $m\in[1;N_s]$ [elements (a) of Fig. 3]. For each $m>N_s$ the sum is split into two sums, Eq. (16). $E_f^{m,(\mathrm{s})}$ is computed exactly [elements (c)] and $E_f^{m,(\mathrm{w})}$ is computed from SA [elements (b)]. For this purpose, $F_m(\phi_p)$ is found from $F_{m-1}(\phi_p)$ for every $p\in[-Q;Q]$ using Eq. (20) with $\Delta\phi=2\phi_{\max}/(2Q+1)\in\mathbb{R}$, and then summed over p. Initially, $F_m(\phi_p)=0$ for $m\in[1;N_s+1]$.

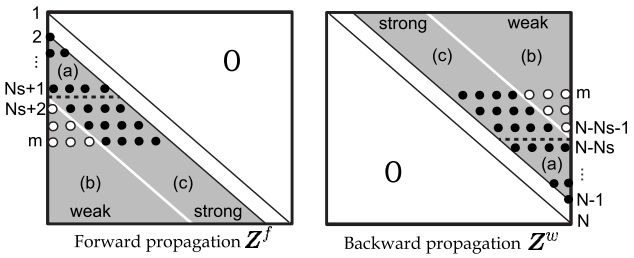

Fig. 3. Illustration of steps for the product $\bar{\mathbf{B}}_f\mathbf{v}_2$ (left) and $\bar{\mathbf{B}}_b\mathbf{v}_2$ (right), where $\mathbf{v}_2=\mathbf{v}_{2f}+\mathbf{v}_{2b}$. First, the elements of domain (a) are multiplied by $\mathbf{v}_2$ exactly. Then elements (b) and (c) are multiplied by $\mathbf{v}_2$ with those of (b) using the SA algorithm and those of (c) exactly as for (a).

In Eq. (15), the sum $\Sigma_{n=1}^{n=m-1}D_f^{m,n}u_2^n$ is computed in the same manner as $\Sigma_{n=1}^{n=m-1}B_f^{m,n}u_2^n$ by substituting K_1 for K_2 in Eqs. (18)–(20).

For the backward steps, the sums $\Sigma_{n=m+1}^{n=N}B_b^{m,n}u_2^n$ and $\Sigma_{n=m+1}^{n=N}C_b^{m,n}u_2^n$ must be computed. The main difference is that $x_m-x_n<0$ so the decomposition of the Green function is the same as Eq. (17), but $\sin\phi$ is replaced by $-\sin\phi$. In a practical way, the consequence on Eqs. (18)–(20) is that $\cos\phi$ is unchanged, but $\sin\phi\rightarrow-\sin\phi$. Furthermore, in Eq. (19) the summation goes from $m+N_s+1$ to N_+, and in Eq. (20), F_m is obtained from F_{m+1}.

2. TM Case

For the TM case, the products $A_f^{m,n}u_1^n$ and $C_f^{m,n}u_1^n$ are involved. From Eq. (A3), the elements of the matrix $\bar{\mathbf{A}}=\bar{\mathbf{A}}_+$ are expressed from the 2D Green function as $A^{m,n}=-\Delta x_+\partial g_1(\mathbf{r}_+^m,\mathbf{r}_+^n)/\partial n_+$ expressed from the Hankel function. Thus, from Eq. (17), we have

$$\frac{\partial g_1(\mathbf{r}_+^m,\mathbf{r}_+^n)}{\partial n_+}=-\frac{K_1}{4\pi}\int_C \exp\{jK_1[(x_+^m-x_+^n)\cos\phi + (z_+^m-z_+^n)\sin\phi]\}(\gamma_+^n\cos\phi-\sin\phi)\mathrm{d}\phi, \tag{21}$$

with $\gamma_+=\partial z_+/\partial x_+$. The same algorithm as in the previous TE case can be applied for both forward and backward steps. The differences are in the expressions of F_m in Eq. (19) and in the recurrence relation Eq. (20). We have

$$F_m(\phi)=\sum_{n=1}^{m-N_s-1}u_1^n\exp\{jK_1[(x_+^m-x_+^n)\cos\phi+(z_+^m-z_+^n)\sin\phi]\}\times(\gamma_+^n\cos\phi-\sin\phi), \tag{22}$$

and

$$F_m(\phi)=F_{m-1}(\phi)\exp(jK_1\Delta x_+\cos\phi)+(\gamma_+^{m-N_s-1}\cos\phi-\sin\phi)u_1^{m-N_s-1}\times\exp\{jK_1[(N_s+1)\Delta x_+\cos\phi-z_+^{m-N_s-1}\sin\phi]\}. \tag{23}$$

The same term $(\gamma_+^n\cos\phi-\sin\phi)$ is also applied as a factor for the backward step.

3. New Contour Integration C_δ

As shown at the top (frequency domain) of Fig. 2, the SA method substitutes for the integration contour C_g a steepest descent path $C^{\{m,n\}}$ going through the saddle point $\phi_s^{m,n}=\arctan[(z_+^m-z_+^n)/(x_+^m-x_+^n)]\in[-\pi/2;+\pi/2]$. The group of paths $C^{\{m,n\}}$ associated with all pairs of points $(\mathbf{r}_+^m,\mathbf{r}_+^n)$ can be replaced by a unique path C_δ going through the origin. Furthermore, close to the origin, C_δ is a straight line having a slope $-\tan\delta$. If δ is correctly chosen, the integrands of Eqs. (17) and (21) decay rapidly away from the origin and the phase has little variation. Thus, as in a classical saddle-point technique, after replacing $C^{\{m,n\}}$ by C_δ in Eqs. (17) and (21), the integration over ϕ can be approximated by a sum over a limited number of complex angles $\phi_p\exp(-j\delta)=p\Delta\phi\exp(-j\delta)$ with $\Delta\phi=2\phi_{\max}/(2Q+1)\in\mathbb{R}$ and $p\in[-Q;Q]$ an integer.

The parameters $\{\phi_{\max},\tan\delta\}$ that define the integration contour C_δ are then given by

$$\phi_{\max}=\min\left(\frac{\phi_{s,\max}}{2}+\sqrt{\frac{\phi_{s,\max}^2}{4}+\frac{b_s}{K_1r_{d0}\tan\delta_0}};\frac{\pi}{2}\right)\quad b_s=6, \tag{24}$$

$$\tan\delta=\min\left(\frac{4a_s}{K_1r_{d0}\phi_{s,\max}^2};1\right)\quad a_s=5, \tag{25}$$

$$\phi_{s,\max}=\arctan\left[\frac{z_+^{\max}-z_+^{\min}}{x_{d0}}\right], \tag{26}$$

$$r_{d0}=\sqrt{x_{d0}^2+(z_+^{\max}-z_+^{\min})^2}, \tag{27}$$

with $z_+^{\max}=\max(z_+)$ and $z_+^{\min}=\min(z_+)$. A detailed study of the calculation of these parameters can be found in [25]. Physically, in the spatial domain (bottom of Fig. 2), $\phi_{s,\max}$ corresponds to the maximum angle defined with respect to $\hat{\mathbf{x}}$ at which the current point sees the other points on the surface. This corresponds to the illuminated zone or the strong interaction zone. For this region, the angles $\phi^{m,n}$ are close to the saddle point $\phi_s^{m,n}$, and the imaginary part of $\phi^{m,n}$ is small. The associated waves are propagated.

On the other hand, if $\phi_s^{m,n}>\phi_{s,\max}\in\mathbb{R}$, the imaginary part of $\phi^{m,n}$ becomes larger and the associated waves are not propagated (evanescent waves). This corresponds to the shadowed zone or the weak interaction zone. From Eqs. (26) and (27), the horizontal distance x_{d0} separating the weak from the strong interactions must be known. From the bottom of Fig. 2, x_{d0} corresponds to the distance separating two points of the surface having, respectively, a large and small height. Thus, statistically x_{d0} must be of the order of the surface height correlation length L_c. Simulations done on the single rough interface showed that x_{d0} ranges from $2L_c$ to $3L_c$. In addition $Q=16$, which means for the weak interactions that the Hankel function can be approximated as $2Q+1=33$ plane waves of propagation angles $\phi_p\exp(-j\delta)$.

4. Complexity and Memory Space for PILE+FB-SA

From Eqs. (20) and (23), the number of multiplications are, respectively, $2(2Q+1)(N_+-N_s)$ and $3(2Q+1)(N_+-N_s)$,

and from Eq. (18), $(2Q+1)(N_+-N_s)$ for each polarization. Thus, for an iteration number P_{FB} of the FB, the backward and forward steps applied on the four submatrices lead to $(3+4)(2Q+1)(N_+-N_s)\times 2\times 2P_{\mathrm{FB}}$ for the weak interactions, and $4N_+N_s$ for the strong interactions. A direct LU inversion of $\bar{\mathbf{Z}}_-$ leads to $N_-^3/3$ multiplications. So the computation of the characteristic matrix (10) requires $8N_+N_-+2N_-2N_-$ of the matrix-vector products, and $N_-^3/3+[28(2Q+1)(N_+-N_s)+4N_+N_s]P_{\mathrm{FB}}$ of the inversions.

In conclusion, from Eq. (8), $\mathbf{X}_+$ at the order P_{PILE} with PILE combined with FB-SA needs

$$\begin{aligned}&\{8N_+N_- + 4N_-^2(\text{matrix-vector products})\\&+[28(2Q+1)(N_+-N_s)\\&+4N_+N_s]P_{\mathrm{FB}}(\text{inversion of }\bar{\mathbf{Z}}_+)\}P_{\mathrm{PILE}}\\&+[28(2Q+1)(N_+-N_s)\\&+4N_+N_s]P_{\mathrm{FB}}(\text{order 0, inversion of }\bar{\mathbf{Z}}_+)\\&+(2N_-)^3/3(\text{initialization:inversion of }\bar{\mathbf{Z}}_-)\end{aligned}\tag{28}$$

operations, instead of $(2N_+)^3/3+(2N_-)^3/3+4N_+^2+(8N_+N_-+4N_+^2+4N_-^2)P_{\mathrm{PILE}}$ from PILE. At the order 0, since $N_+\gg N_s$ and $N_+\gg 1$, PILE+FB-SA is fast compared to PILE if $(2N_+)^2/3\gg[28(2Q+1)+4N_s]P_{\mathrm{FB}}$. Typically, $N_s=100$, $P_{\mathrm{FB}}=8$, $Q=16$, thus $N_+\gg 22$. At the order P_{PILE}, we must have $N_+\gg[28(2Q+1)+4N_s]P_{\mathrm{FB}}/4$, which leads to $N_+\gg 2648$. But the storage of the inverse of $\bar{\mathbf{Z}}_+$ is not necessary, unlike in PILE. Indeed with FB-SA, only the submatrix elements of $\bar{\mathbf{Z}}_+$ of the strong interactions must be stored. For a submatrix, the number of elements is $N_s(N_s+1)/2+(N_+-N_s-1)N_s$, which leads to N_+N_s for $N_+\gg N_s$ instead of N_+^2.

3. NUMERICAL RESULTS

In this section, the PILE method combined with FB-SA and referred to as PILE+FB-SA is compared with the results obtained from a direct LU inversion of the impedance matrix $\bar{\mathbf{Z}}$. The input parameter of PILE is its order P_{PILE} [see Eq. (8)], which is related to the number of reflections between the object and the rough surface. The input parameters of PILE+FB are P_{PILE} and the order P_{FB} of the FB method for the inversion of the impedance matrix of the rough surface. Eventually, the input parameters of PILE+FB-SA are P_{PILE}, P_{FB}, and x_{d0}, which is the distance of the strong interactions required for the calculation of the integration contour C_δ. One of the advantages of the PILE method is the separation of the local interactions of the rough surface [related to $\bar{\mathbf{Z}}_+^{-1}$ in Eq. (10)] and those of the object [related to $\bar{\mathbf{Z}}_-^{-1}$ in Eq.(10)]. Thus, a means to obtain the parameters P_{FB} and x_{d0} is to study the scattering from a single rough dielectric interface (without the object); this is the purpose of Subsection 3.A. In Subsections 3.B and 3.C, the convergences of PILE and PILE+FB-SA are investigated, while Section 4 presents the computation time of PILE+FB-SA.

A. Determination of the Parameters P_{FB} and x_{d0}

For all simulations, the order P_{FB} is obtained when the relative residual error (RRE) r_e, defined as

$$\mathrm{RRE}: r_e = \frac{\mathrm{norm}(\mathbf{X}-\mathbf{X}_{\mathrm{LU}})}{\mathrm{norm}(\mathbf{X}_{\mathrm{LU}})},\tag{29}$$

is smaller than a threshold chosen as 10^{-3} in what follows. The norm of a vector of components X_i and of length N is expressed as $\mathrm{norm}(\mathbf{X})=\Sigma_{i=1}^{i=N}|X_i|^2$. $\mathbf{X}$ represents either the field ψ or its normal derivative $\partial\psi/\partial n$ on the surface. The subscript LU means that the vector is computed from a LU inversion (benchmark solution). The order P_{FB} is then obtained when r_e becomes smaller than 10^{-3}. Since r_e is determined for ψ and $\partial\psi/\partial n$, we take the largest value of P_{FB}. In what follows, the surface is assumed to be a Gaussian process with a Gaussian height spectrum, and the incident medium Ω_1 is the vacuum (the incident wavelength is denoted as λ_0).

Table 1 presents the order P_{FB} for a single rough dielectric surface and for the TE and TM polarizations. It is computed from one surface realization. The correlation length is $L_c=2\lambda_0$, the RMS heights are $\sigma_z\in[0.1;2]\lambda_0$ (RMS slope $\sigma_\gamma=\sqrt{2}\sigma_z/L_c\in[0.0707;1.4142]$). The sampling step is $\lambda_0/10$, the surface length $L_+=120\lambda_0$ ($N_+=1200$), and Thorsos' wave parameter $g=L/6$. We can note that the FB method converges fast for $\epsilon_{r2}=2+0.01j$ [(a) and (b) cases], and the order P_{FB} is quite insensitive to the RMS height and the incidence angle. In addition, as $|\epsilon_{r2}|$ increases, the order FB increases for the TE polarization, whereas it remains unchanged for the TM polarization.

In Fig. 4, the scattering coefficient in dB scale is compared with that obtained from a direct LU inversion versus the scattering angle θ_s. From Thorsos' wave and for $\mathbf{r}\in\Omega_1$, it is equal to [10]

$$\sigma_s(\theta_i,\theta_s)=\frac{|\psi_\infty|^2}{8\pi K_0 g\cos\theta_i\left[1-\dfrac{1+2\tan^2\theta_i}{2K_0^2g^2\cos^2\theta_i}\right]},\tag{30}$$

with

$$\psi_\infty=\int_{\Sigma_+}\left\{\frac{\partial\psi_+}{\partial n_+}\sqrt{1+\gamma_+^2}-jK_0\psi_+[\gamma_+\sin\theta_s-\cos\theta_s]\right\}e^{-j\mathbf{k}_s\cdot\mathbf{r}}\mathrm{d}x_+,\tag{31}$$

with $\mathbf{k}_s=K_0(\hat{\mathbf{x}}\sin\theta_s+\hat{\mathbf{z}}\cos\theta_s)$ $(K_0=2\pi/\lambda_0)$ the scattering wave vector and $\gamma_+=\partial z_+/\partial x_+$. At the top is the TE case and at the bottom, the TM case. The parameters are the

Table 1. Order P_{FB} for a Single Rough Dielectric Surface (without Object) and for the TE and TM Polarizations[a]

σ_z/λ_0	0.1	0.5	1	1.5	2
$\theta_i(^\circ)$, ϵ_{r2}	TE,TM	TE,TM	TE,TM	TE,TM	TE,TM
(a) 0, 2+0.01j	7,6	7,6	7,7	8,7	10,9
(b) 60, 2+0.01j	8,7	8,7	8,7	8,7	9,9
(c) 0, 10+j	12,8	12,7	13,7	15,8	14,8

[a]Three cases are considered. Correlation length $L_c=2\lambda_0$, sampling step $\lambda_0/10$, surface length $L_+=120\lambda_0$ ($N_+=1200$), and Thorsos' wave parameter $g=L_+/6$.

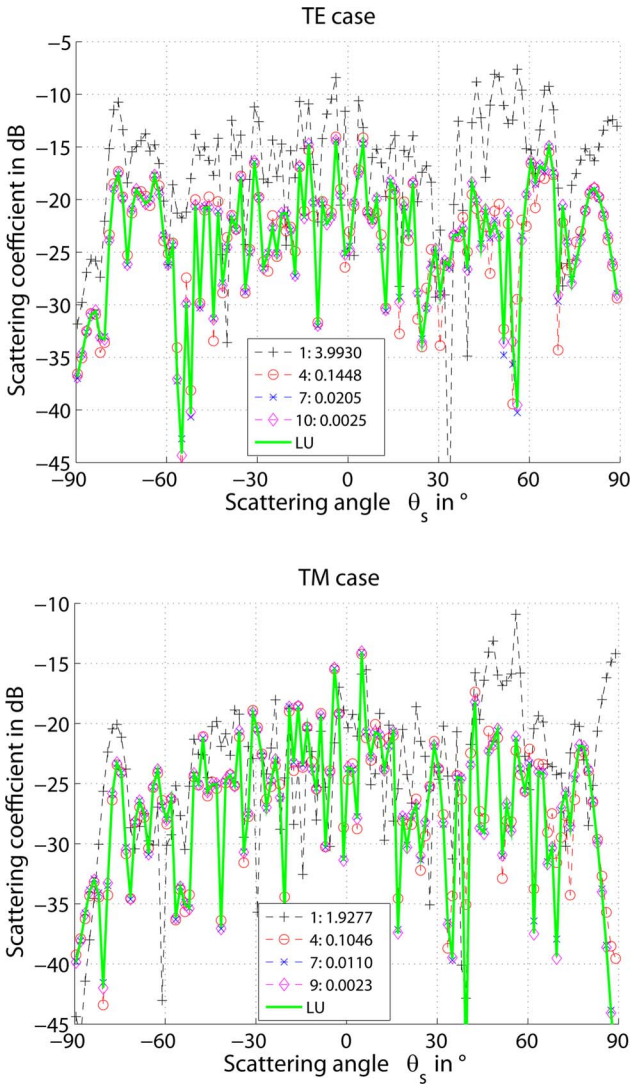

Fig. 4. (Color online) Comparison of the scattering coefficient (without object) in dB scale with that obtained from a direct LU inversion versus the scattering angle θ_s. Top, TE case; bottom, TM case. In the legends, the order P_{FB} and the RRE in linear scale of the scattering coefficients are given. The parameters are the same as in Table 1 with $\epsilon_{r2}=2+0.01j$, $\theta_i=0°$ and $\sigma_z=2\lambda_0$ [(a) case].

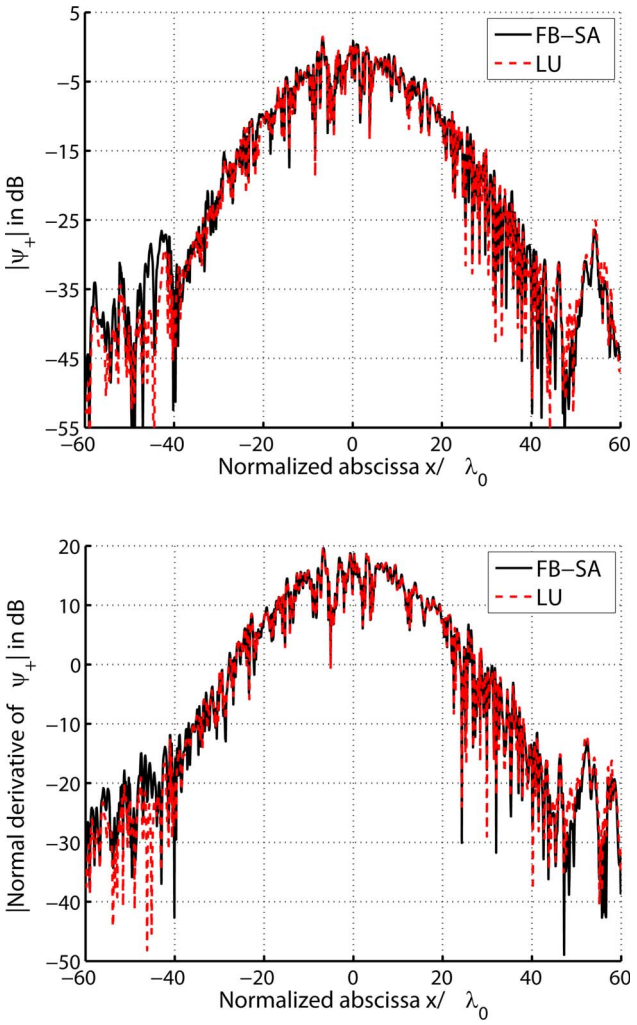

Fig. 5. (Color online) Comparison of the field $|\psi_+|$ and its normal derivative $|\partial\psi_+/\partial n_+|$ (without object) on the surface computed from FB-SA with those obtained from a direct LU inversion versus the normalized abscissa x/λ_0 and for the TE case. The parameters are the same as in Fig. 4 with $x_{d0}=3L_c$ and the order P_{FB} is taken from Table 1.

same as in Table 1 with $\epsilon_{r2}=2+0.01j$, $\theta_i=0°$, and $\sigma_z=2\lambda_0 \Rightarrow \sigma_\gamma=\sqrt{2}$ [in the (a) case]. As the order P_{FB} increases, the RRE decreases and we can observe that the results converge toward those obtained from a direct LU inversion. The last order is taken from Table 1.

Like the PILE method, Déchamps *et al.* [28] have recently shown that the FB method converges if the norm (the modulus of its eigenvalue that has the highest modulus) of the characteristic matrix

$$\bar{\mathbf{M}}_{\mathrm{FB}}=(\bar{\mathbf{Z}}_{+,d}+\bar{\mathbf{Z}}_{+,f})^{-1}\bar{\mathbf{Z}}_{+,f}(\bar{\mathbf{Z}}_{+,d}+\bar{\mathbf{Z}}_{+,b})^{-1}\bar{\mathbf{Z}}_{+,b} \tag{32}$$

is smaller than one. $\bar{\mathbf{Z}}_{+,d}$ is a matrix of size $2N_+\times 2N_+$ built from the diagonal of the matrices $\bar{\mathbf{A}}$, $\bar{\mathbf{B}}$, $\bar{\mathbf{C}}$ and $\bar{\mathbf{D}}$ (see Appendix A) of sizes $N_+\times N_+$. In the same manner, $\{\bar{\mathbf{Z}}_{+,f},\bar{\mathbf{Z}}_{+,b}\}$ are matrices of sizes $2N_+\times 2N_+$ built from the lower and upper triangular matrices with zero values on the diagonal of $\bar{\mathbf{A}}$, $\bar{\mathbf{B}}$, $\bar{\mathbf{C}}$, and $\bar{\mathbf{D}}$, respectively ($\bar{\mathbf{Z}}_+=\bar{\mathbf{Z}}_{+,f}+\bar{\mathbf{Z}}_{+,d}+\bar{\mathbf{Z}}_{+,b}$). The norm of $\bar{\mathbf{M}}_{\mathrm{FB}}$ [norm($\bar{\mathbf{M}}_{\mathrm{FB}}$)] is a relevant criterion to study the validity of FB because it is independent of the incidence and scattering angles. It depends only on the surface profile and the permittivity ϵ_{r2}. For a single dielectric rough surface, Iodice [30] has studied in detail the convergence of the FB against the choice of the height autocorrelation function (HAF). For a Gaussian HAF, the FB always converges, whereas for an exponential HAF with the same correlation length and RMS height as the Gaussian case, the FB may fail for very rough surfaces. For example, with $N_+=800$, $L_+=80\lambda_0$, $L_c=2\lambda_0$, $\sigma_z=\lambda_0$, $\epsilon_{r2}=2+0.01j$, $g=L_+/6$, norm($\bar{\mathbf{M}}_{\mathrm{FB}}$)$=0.4114<1$ for a Gaussian HAF, whereas norm($\bar{\mathbf{M}}_{\mathrm{FB}}$)$=2.7662>1$ for an exponential HAF, which means that the FB method does not converge in that case. This is verified if we compute the scattering coefficient for different incidence and scattering angles.

In Fig. 5 the field $|\psi_+|$ and its normal derivative $|\partial\psi_+/\partial n_+|$ on the surface computed from FB-SA are com-

pared with those obtained from a direct LU inversion versus the normalized abscissa x/λ_0 for the TE case. The parameters are the same as in Fig. 4 and the order P_{FB} is taken from Table 1. The distance of the strong interaction is $x_{d0}=3L_c=6\lambda_0$. We observe a very good agreement. From the parameters of Table 1, similar simulations with $x_{d0}=3L_c$ and for TE and TM polarizations, not reported in this paper, also showed very good agreement. In conclusion, in what follows x_{d0} will be set equal to $3L_c$ for the spectral acceleration.

B. Convergence of PILE

The purpose of this subsection is to study the convergence of PILE versus its order P_{PILE}. In what follows, the abscissa of the object is $x_c=0$, and a will denote the radius of a circular cylinder and h_c its depth.

In Fig. 6, for the TE case, the modulus of the field ψ_+ on the rough surface is plotted versus the normalized abscissa x/λ_0. The parameters are $\theta_i=0°$, $L_c=2\lambda_0$, $\sigma_z=\lambda_0$, $\epsilon_{r2}=2+0.01j$, sampling step $\lambda_0/10$ ($N_+=1200$) for the rough surface of length $L_+=120\lambda_0$, $g=L_+/6$, $N_-=126$ ($\Delta r_-\approx a\Delta\phi=0.1\lambda_0$), $h_c=4\lambda_0$, and $a=2\lambda_0$. At the top is shown the PILE method; middle, PILE+FB method with $P_{\mathrm{FB}}=7$ obtained from Table 1, bottom, PILE+FB-SA method with $x_{d0}=3L_c$. In each subfigure, the order of PILE and the corresponding RRE are noted in the legend. In addition, the results computed from a direct LU inversion are plotted.

At the top (see Subsection 3.C for a discussion of PILE+FB and PILE+FB-SA), we can observe that the PILE method converges after three iterations, which means that the number of reflections between the surface and the object in medium Ω_2 contributing to the scattering process is $P_{\mathrm{PILE}}=3$. $P_{\mathrm{PILE}}=0$ gives the contribution to the scattering from only the rough surface. In addition, Fig. 6 reveals that the field vanishes on the edges of the surface. This condition must be satisfied to apply the integral equations.

Figure 7 presents, for different orders P_{PILE}, the modulus of the radiated field $\psi_{\mathrm{rad}}(\mathbf{r})$ computed from the fields on the rough surface and the object versus the normalized abscissa x/λ_0 and the normalized height h/λ_0 for the TE polarization. It is expressed as

$$\psi_{\mathrm{rad}}(\mathbf{r})=-\sum_{p=\pm}s_p\int_{\Sigma_p}\left[\psi_p(\mathbf{r}_p)\frac{\partial g_p(\mathbf{r}_p,\mathbf{r})}{\partial n_p}-g_p(\mathbf{r}_p,\mathbf{r})\frac{\partial\psi_p(\mathbf{r}_p)}{\partial n_p}\right]\mathrm{d}\Sigma_p, \tag{33}$$

with $\mathbf{r}\notin(\Sigma_+\cup\Sigma_-)$ (and Ω_3 if the object is a perfect conductor); $\{s_-=0,s_+=1\}$ if $\mathbf{r}\in\Omega_1$, otherwise $\{s_\pm=+1\}$; and $g_p(\mathbf{r}_p,\mathbf{r})=j/4H_0^{(1)}(K_0\sqrt{\epsilon_{rp}}\|\mathbf{r}_p-\mathbf{r}\|)$, in which $\epsilon_{rp}=\epsilon_{ri}$ if $\mathbf{r}\in\Omega_i$. The parameters are the same as in Fig. 6, but $\sigma_z=0.5\lambda_0$, $L_+=80\lambda_0$, $\theta_i=30°$, and $g=L_+/4$. Figure 7 clearly shows that the PILE order is related to the number of reflections into the medium Ω_2.

With the same parameters as in Fig. 6, except for $a=\{0.5,1,2,3\}\lambda_0\Rightarrow N_-=\{31,63,126,188\}$ and $\sigma_z=0.5\lambda_0$, simulations showed that the order of PILE is $P_{\mathrm{PILE}}=\{2,3,3,3\}$ for the TE polarization, whereas for the TM case, $P_{\mathrm{PILE}}=\{2,2,3,3\}$.

Table 2 presents the order P_{PILE} for a circular cylinder below a rough dielectric surface and for the TE and TM polarizations. It is computed from one surface realization. The parameters are $L_c=2\lambda_0$, $\sigma_z\in[0.1;2]\lambda_0$, sampling step

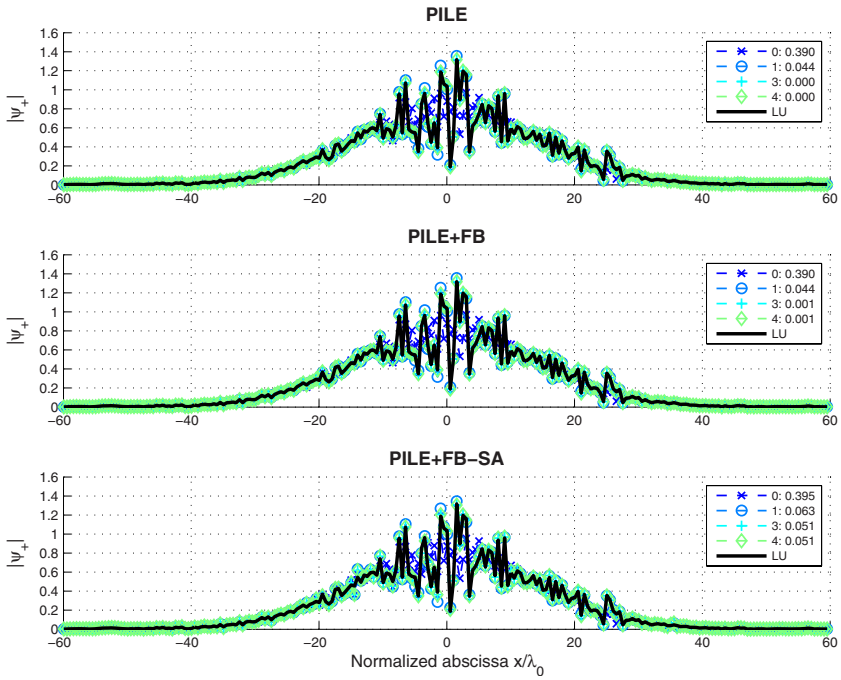

Fig. 6. (Color online) Modulus $|\psi_+|$ of the rough surface versus the normalized abscissa x/λ_0 for the TE case. $\theta_i=0°$, $L_c=2\lambda_0$, $\sigma_z=\lambda_0$, $\epsilon_{r2}=2+0.01j$, $N_+=1200$, $L_+=120\lambda_0$, $g=L_+/6$, $N_-=126$, $h_c=4\lambda_0$, and $a=2\lambda_0$. Top, PILE method. Middle, PILE+FB method with $P_{\mathrm{FB}}=7$. Bottom, PILE+FB-SA method with $x_{d0}=3L_c$. In each subfigure, the order of PILE and the corresponding RRE are given in the legend. In addition, the results computed from a direct LU inversion are plotted.

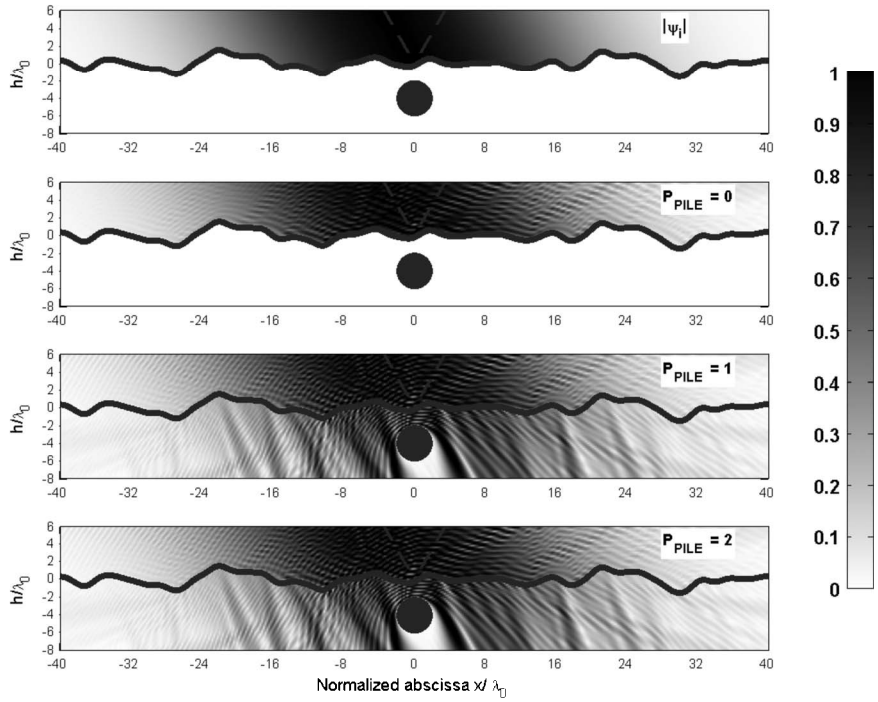

Fig. 7. Modulus of the radiated field computed from the fields on the rough surface and the object versus the normalized abscissa x/λ_0 and the normalized height h/λ_0 for the TE polarization and for different orders P_{PILE}. The parameters are the same as in Fig. 6, but $\sigma_z=0.5\lambda_0$, $L_+=80\lambda_0$, $\theta_i=30°$, and $g=L_+/4$.

$\lambda_0/10$ for the rough surface of length $L_+=120\lambda_0$ ($N_+=1200$), Thorsos' wave parameter $g=L_+/6$, $N_-=126$, $h_c=4\lambda_0$, and $a=2\lambda_0$. Three cases are considered. As the modulus of the permittivity $|\epsilon_{r2}|$ increases, the order P_{PILE} decreases. Indeed, the skin depth δ decreases when $|\epsilon_{r2}|$ increases ($\epsilon_{r2}=\{2+0.01j, 10+j\} \Rightarrow \delta=\{45,1\}\lambda_0$), which implies that the number of reflections between the rough surface and the object contributing to the scattering decreases. Table 2 reveals also that P_{PILE} is independent of the incidence angle θ_i and the polarization.

Table 3 presents the order P_{PILE} for an elliptic cylinder below a rough dielectric surface and for the TE and TM polarizations. The parameters are $L_c=2\lambda_0$, $\sigma_z=0.5\lambda_0$, sampling step $\lambda_0/10$ for the rough surface of length $L_+=120\lambda_0$ ($N_+=1200$), $\epsilon_{r2}=2+0.01j$, $\theta_i=0°$, $g=L_+/6$, $h_c=4\lambda_0$, and $b=\lambda_0$ (semiminor axis and $a \geq b$). As the semimajor axis a increases, the order P_{PILE} increases slightly, which means that the interactions between the object and the rough surface are stronger.

Table 2. Order P_{PILE} for a Circular Cylinder below a Rough Dielectric Surface and for the TE and TM Polarizations[a]

σ_z/λ_0	0.1	0.5	1	1.5	2
$\theta_i(°)$, ϵ_{r2}	TE,TM	TE,TM	TE,TM	TE,TM	TE,TM
(a) 0, 2+0.01j	3,3	3,3	3,3	3,3	3,3
(b) 60, 2+0.01j	3,3	3,3	3,3	3,3	3,3
(c) 0, 10+j	1,1	1,1	1,1	2,2	3,3

[a]Three cases are considered. Correlation length $L_c=2\lambda_0$, sampling step $\lambda_0/10$ for the rough surface of length $L_+=120\lambda_0$ ($N_+=1200$), Thorsos' wave parameter $g=L_+/6$, $N_-=126$, $h_c=4\lambda_0$, and $a=2\lambda_0$.

C. Convergence of PILE+FB-SA

The parameters of the FB-SA needed to calculate the local interactions on the rough surface are given in Table 1. In addition, the distance of the strong interactions is $x_{d0}=3L_c$.

Figure 6 reveals also that the PILE method combined with FB exhibits a good convergence, which means that the order P_{FB} is well chosen. Nervertheless, the convergence of the PILE+FB-SA approach is not perfect, since the RRE remains constant after 3 iterations. Although the values of the RRE on the first iteration of PILE+FB and PILE+FB-SA are very close, the values at the next iterations differ. This implies that the error propagates with P_{PILE}. But, as displayed in Fig. 8, the impact of this difference on the scattering coefficient is minor except at grazing scattering angles. In the legend, the RRE is given in linear scale.

Figures 9 and 10 compare the RRE over the scattering coefficient against the normalized RMS height σ_z/λ_0 for the TE and TM polarizations, respectively. The order P_{PILE} is obtained from Table 2, from which the (a) case is

Table 3. Order P_{PILE} for an Elliptic Cylinder below a Rough Dielectric Surface and for the TE and TM Polarizations

a/λ_0	1	3	5	7	9
N_-	63	134	210	288	367
P_{PILE} TE	3	3	4	4	4
P_{PILE} TM	2	3	3	3	4

[a]The parameters are $L_c=2\lambda_0$, $\sigma_z=0.5\lambda_0$, sampling step $\lambda_0/10$ for the rough surface of length $L_+=150\lambda_0$ ($N_+=1200$), $\epsilon_{r2}=2+0.01j$, $\theta_i=0°$, $g=L_+/6$, $h_c=4\lambda_0$, $b=\lambda_0$ (semiminor axis and $a \geq b$).

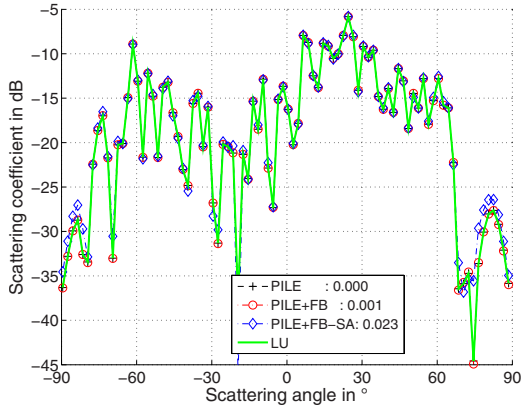

Fig. 8. (Color online) Comparison of the scattering coefficient in dB scale with that obtained from a direct LU inversion versus the scattering angle θ_s. The parameters are the same as in Fig. 6.

considered. As we can see, the RRE is of the order of 10^{-3} for PILE, whereas it is proportional to the RMS height for FB and FB-SA and it is quite insensitive to the polarization. In addition, the RRE is larger for FB-SA.

To study the effect of the distance x_{d0}, in Fig. 11 the RRE over the scattering coefficient is plotted versus x_{d0}/L_c for the TE and TM polarizations. The parameters are the same as in Fig. 6 and the orders are $\{P_{\mathrm{FB}}=7, P_{\mathrm{PILE}}=3\}$ and $\{P_{\mathrm{FB}}=6, P_{\mathrm{PILE}}=3\}$ for the TE and TM

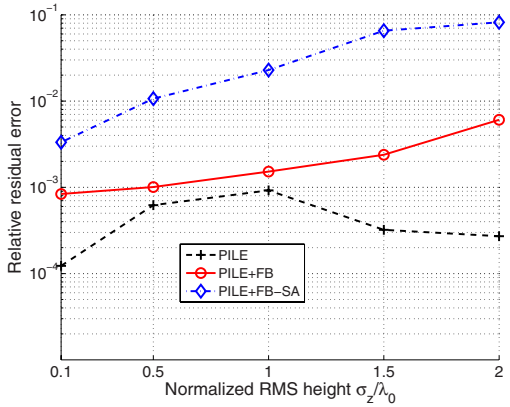

Fig. 9. (Color online) Comparison of the RRE over the scattering coefficient versus the normalized RMS height σ_z/λ_0 for the TE polarization. The order P_{PILE} is obtained from Table 2, from which the (a) case is considered.

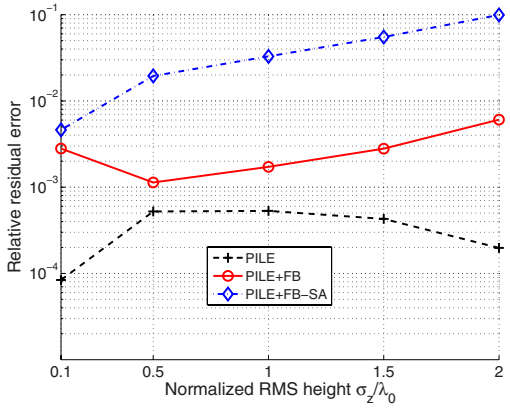

Fig. 10. (Color online) Same variation as in Fig. 9 but for the TM polarization.

polarizations, respectively. We can observe that the RRE decreases slowly with x_{d0} and reaches the value obtained from PILE+FB for $x_{d0} \geq 40L_c$.

D. Computation Time of PILE+FB-SA

In Fig. 12 the CPU time t_{CPU} of the PILE+FB-SA is plotted versus the number of samples N_+ on the rough surface. The parameters are the same as in Fig. 6 with $\{P_{\mathrm{FB}}=7, P_{\mathrm{PILE}}=3\}$ and $\{P_{\mathrm{FB}}=6, P_{\mathrm{PILE}}=3\}$ for the TE and TM polarizations (Tables 1 and 2), respectively. It should be noted that the number of unknowns are $2N_+ + N_- = 2N_+ + 126$. In addition, results obtained from a linear regression (TE case: $t_{\mathrm{CPU}} = -15.7741 + 0.0035N_+$; TM case: $t_{\mathrm{CPU}} = -14.8946 + 0.0032N_+$) are displayed. A 3.4 GHz personal computer with 2 GB of RAM with the MATLAB software is used in this work. We can observe that the CPU time of PILE+FB-SA is approximately proportional to N_+. Nevertheless, the CPU time for the TE polarization is larger because the product $P_{\mathrm{FB}}P_{\mathrm{PILE}}$ is larger than that obtained from the TM polarization. In fact, the ratio of the slope of the regression straight line for each polarization is approximately equal to the ratio computed from $P_{\mathrm{FB}}(P_{\mathrm{PILE}}+1)$. Thus, as expected, the CPU time is of the order of $P_{\mathrm{FB}}(P_{\mathrm{PILE}}+1)\mathcal{O}(N_+)$.

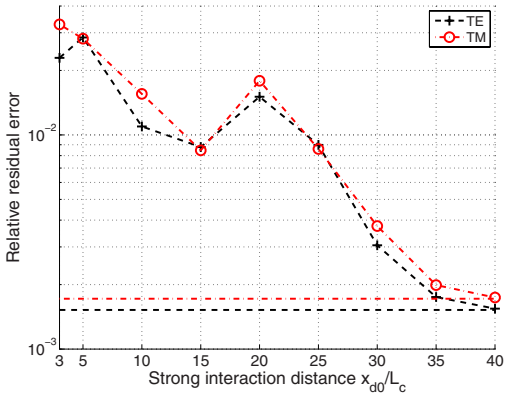

Fig. 11. (Color online) RRE over the scattering coefficient of PILE+FB-SA versus the normalized distance x_{d0}/L_c for the TE and TM polarizations. The parameters are the same as in Fig. 6. The horizontal lines indicate the values of RRE of PILE+FB obtained from Figs. 9 and 10 with $\sigma_z = \lambda_0$.

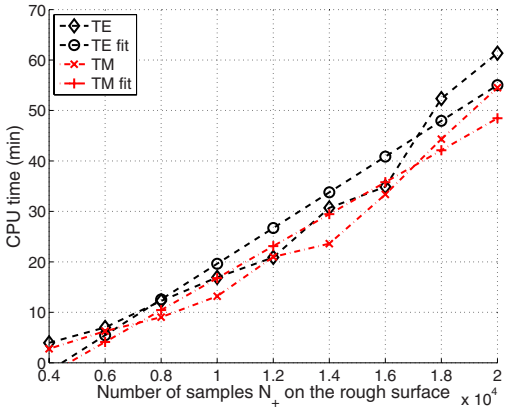

Fig. 12. (Color online) CPU time versus the number of samples N_+ on the rough surface. The parameters are the same as in Fig. 6 with $\{P_{\mathrm{FB}}=7, P_{\mathrm{PILE}}=3\}$ and $\{P_{\mathrm{FB}}=6, P_{\mathrm{PILE}}=3\}$ for the TE and TM polarizations (Tables 1 and 2), respectively. The number of unknowns is $2N_+ + N_- = 2N_+ + 126$.

One of the advantages of PILE+FB-SA is the capability of treating large problems with a personal computer. For instance, for $N_+=20{,}000$ and $N_-=126$, the number of unknowns is 40,126. In this case, the PILE+FB-SA requires storing 126^2 (for $\bar{\mathbf{Z}}_-$) plus $3\times126\times20{,}000$ (coupling matrices) plus $4\times2\times1{,}198{,}170$ $(8N_s[(N_s+1)/2+(N_+-N_s-1)]$ strong interactions for $\bar{\mathbf{Z}}_+$ (with $N_s=60$) = 17,161,236 complex values, which corresponds to $2\times16\times17{,}161{,}236/8/1024^2\approx66$ megabytes of memory.

4. CONCLUSION

We have presented a new efficient method to predict the field scattered from a homogeneous object located below a one-dimensional (1-D) dielectric rough surface. The method is based on the rigorous PILE method, originally developed for a stack of two 1-D rough interfaces separating homogeneous media and updated in this work to an object beneath a surface. In addition, for the calculation of the local interactions of the rough surface, the PILE method was accelerated using the fast method of forward-backward (FB), combined with a spectral acceleration (SA). The resulting method, the PILE+FB-SA, has then a complexity of $\mathcal{O}(N_+)$, in which N_+ is the number of samples on the rough surface, if $N_+\gg N_-$ (number of the samples on the object).

The numerical results showed that the PILE method converges fast. Indeed, the PILE order corresponds to the number of reflections between the object and the rough surface contributing to the scattering process. Combined with FB, the PILE+FB also converges quickly for the FB step (after 7–8 iterations for $\epsilon_{r2}=2+0.01j$ and 12–15 iterations for $\epsilon_{r2}=10+j$; see Table 1). One of the advantages of PILE+FB is that the order P_{FB} of the FB step can be obtained from the study of the scattering from a single rough surface. PILE+FB combined with SA exhibits good convergence for a quite rough surface with a distance of strong interactions of the order of $3L_c$ (height correlation length). As the surface roughness increases (RMS height), this distance must be increased.

Instead of using the FB-SA approach to accelerate the calculation of the local interactions on the rough surface, the banded-matrix-iterative-approach/canonical grid (BMIA-CAG) developed by Tsang *et al.* [21,22] could be applied. This method, of complexity $\mathcal{O}(N_+\log N_+)$ is attractive for RMS heights approximately smaller than $3\lambda_0$. Moreover, as prospects for further research, it could be interesting to study the PILE+FB-SA for an object above a rough surface [31] and for several objects above and below a rough surface.

APPENDIX A: SUBMATRIX EXPRESSIONS OF THE IMPEDANCE MATRIX

For a dielectric object located below a dielectric surface, the submatrices $\{\bar{\mathbf{Z}}_+,\bar{\mathbf{Z}}_-,\bar{\mathbf{Z}}_\pm,\bar{\mathbf{Z}}_\mp\}$ are expressed from elementary submatrices as

$$\bar{\mathbf{Z}}_+=\begin{bmatrix}\bar{\mathbf{A}}_+ & \bar{\mathbf{B}}_+\\ \bar{\mathbf{C}}_+ & \rho_{21}\bar{\mathbf{D}}_+\end{bmatrix},\quad \bar{\mathbf{Z}}_-=\begin{bmatrix}\bar{\mathbf{A}}_- & \bar{\mathbf{B}}_-\\ \bar{\mathbf{C}}_- & \rho_{32}\bar{\mathbf{D}}_-\end{bmatrix},\tag{A1}$$

$$\bar{\mathbf{Z}}_\pm=\begin{bmatrix}\bar{\mathbf{A}}_\pm & \rho_{21}\bar{\mathbf{B}}_\pm\\ \bar{\mathbf{0}} & \bar{\mathbf{0}}\end{bmatrix},\quad \bar{\mathbf{Z}}_\mp=\begin{bmatrix}\bar{\mathbf{0}} & \bar{\mathbf{0}}\\ \bar{\mathbf{A}}_\mp & \bar{\mathbf{B}}_\mp\end{bmatrix},\tag{A2}$$

in which $\{\rho_{21}=\epsilon_{r2}/\epsilon_{r1},\rho_{32}=\epsilon_{r3}/\epsilon_{r2}\}$ for TM polarization, and $\{\rho_{21}=\rho_{32}=1\}$ for TE polarization.

The elementary square matrix $\bar{\mathbf{A}}_+$ (size $N_+\times N_+$) corresponds to the matrix of a perfectly conducting surface for TM polarization (Neumann boundary condition). The elements are given by

$$A_+^{m,n}=\begin{cases}-\dfrac{jK_1\Delta x_+}{4}\dfrac{H_1^{(1)}(K_1\|\mathbf{r}_+^n-\mathbf{r}_+^m\|)}{\|\mathbf{r}_+^n-\mathbf{r}_m^+\|}[\gamma_+^n(x_+^n-x_+^m)-(z_+^n-z_+^m)] & \text{for } m\neq n,\\ +\dfrac{1}{2}-\dfrac{\Delta x_+}{4\pi}\dfrac{(\gamma_+^m)'}{1+(\gamma_+^m)^2} & \text{for } m=n,\end{cases}\tag{A3}$$

with $\gamma_+=\partial z_+/\partial x_+$, $(\gamma_+)'=\partial\gamma_+/\partial x_+$, and $H_1^{(1)}$ the Hankel function of first order and first kind. $K_1=K_0\sqrt{\epsilon_{r1}}$ is the wavenumber in the incident medium Ω_1, and K_0 stands for the wavenumber in vacuum.

The elementary square matrix $\bar{\mathbf{B}}_+$ (size $N_+\times N_+$) corresponds to the matrix of a perfectly conducting surface for TE polarization (Dirichlet boundary condition). The elements are given by

$$B_+^{m,n}=\frac{j\Delta x_+\alpha_+^n}{4}\begin{cases}1+\dfrac{2j}{\pi}\ln(0.164K_1\alpha_+^m\Delta x_+) & \text{for } n=m\\ H_0^{(1)}(K_1\|\mathbf{r}_+^n-\mathbf{r}_+^m\|) & \text{for } n\neq m\end{cases},\tag{A4}$$

with $\alpha_+^n=[1+(\gamma_+^n)^2]^{1/2}$. The elementary matrices $\{\bar{\mathbf{C}}_+,\bar{\mathbf{D}}_+\}$ are obtained from $\{\bar{\mathbf{A}}_+,\bar{\mathbf{B}}_+\}$ by substituting in Eqs. (A3) and (A4), K_1 for K_2. In addition, the diagonal elements of $\bar{\mathbf{C}}_+=-1/2-\Delta x_+/4\pi(\gamma_+^m)'/[1+(\gamma_+^m)^2]$.

The elementary matrices of the object $\{\bar{\mathbf{A}}_-,\bar{\mathbf{B}}_-,\bar{\mathbf{C}}_-,\bar{\mathbf{D}}_-\}$ of size $N_-\times N_-$ are obtained from $\{\bar{\mathbf{A}}_+,\bar{\mathbf{B}}_+,\bar{\mathbf{C}}_+,\bar{\mathbf{D}}_+\}$ by substituting in Eqs. (A3) and (A4), (K_1, K_2, subscript +) for (K_2, K_3, subscript −), respectively. For a buried elliptic cylinder of parametric equations $\{x_-=x_c+a\cos\phi,x_-=-h_c+b\sin\phi\}(h_c>0)$, we must take the absolute values on $|\alpha_-^n\Delta x_-|=\sqrt{a^2\sin^2\phi+b^2\cos^2\phi}|\Delta\phi|$ and $v|\Delta x_-|=v|a\sin\phi\Delta\phi|$, in which $v=+1$ for $\phi\in[0;\pi]$, $v=-1$ otherwise, in order that the normal to the cylinder is always oriented toward the outside of the object. Moreover, $\gamma_-^n=-b/a\cot\phi$.

The coupling matrix $\bar{\mathbf{A}}_\pm$ (size $N_-\times N_+$) is similar to $\bar{\mathbf{A}}_+$ and its elements are expressed as

$$A_\pm^{m,n}=\frac{jK_2\Delta x_+}{4}\frac{H_1^{(1)}(K_2\|\mathbf{r}_+^n-\mathbf{r}_-^m\|)}{\|\mathbf{r}_+^n-\mathbf{r}_-^m\|}[\gamma_+^n(x_+^n-x_-^m)-(z_+^n-z_-^m)].\tag{A5}$$

The coupling matrix $\bar{\mathbf{B}}_\pm$ (size $N_-\times N_+$) is similar to $\bar{\mathbf{B}}_+$ and its elements are expressed as

$$B_{\pm}^{m,n} = -\frac{j\alpha_{+}^{n}\Delta x_{+}}{4} H_0^{(1)}(K_2\|\mathbf{r}_{+}^{n} - \mathbf{r}_{-}^{m}\|). \quad \text{(A6)}$$

The elementary matrices $\{\bar{\mathbf{A}}_{\mp}, \bar{\mathbf{B}}_{\mp}\}$ of size $N_{+}\times N_{-}$ are obtained from $\{\bar{\mathbf{A}}_{\pm}, \bar{\mathbf{B}}_{\pm}\}$ by substituting in Eqs. (A5) and (A6) the subscripts $(+,-)$ for the subscripts $(-,+)$, respectively.

If the object is assumed to be a perfect conductor, then $\bar{\mathbf{Z}}_{\pm}=[\bar{\mathbf{A}}_{\pm} \quad \rho_{21}\bar{\mathbf{B}}_{\pm}]$. Moreover, the submatrices $\{\bar{\mathbf{Z}}_{-}, \bar{\mathbf{Z}}_{\mp}\}$ and the unknown vector $\mathbf{X}_{-}$ become

$$\begin{cases} \text{TE case:} \quad \bar{\mathbf{Z}}_{-} = \bar{\mathbf{B}}_{-}, \bar{\mathbf{Z}}_{\mp} = \begin{bmatrix} \bar{\mathbf{0}} \\ \bar{\mathbf{B}}_{\mp} \end{bmatrix}, \quad \mathbf{X}_{-} \equiv \dfrac{\partial \psi_{-}}{\partial n_{-}} \\ \text{TM case:} \quad \bar{\mathbf{Z}}_{-} = \bar{\mathbf{A}}_{-}, \bar{\mathbf{Z}}_{\mp} = \begin{bmatrix} \bar{\mathbf{0}} \\ \bar{\mathbf{A}}_{\mp} \end{bmatrix}, \quad \mathbf{X}_{-} \equiv \psi_{-} \end{cases}. \quad \text{(A7)}$$

REFERENCES

1. G. Videen and D. Hgo, "Light scattering from a cylinder near a plane interface: theory and comparison with experimental data," J. Opt. Soc. Am. A **14**, 70–78 (1997).
2. T. C. Rao and R. Barakat, "Plane-wave scattering by a conducting cylinder partially buried in a ground plane. I. TM case," J. Opt. Soc. Am. A **6**, 1270–1280 (1989).
3. T. C. Rao and R. Barakat, "Plane-wave scattering by a conducting cylinder partially buried in a ground plane. II. TE case," J. Opt. Soc. Am. A **8**, 1986–1990 (1991).
4. A. Tabatabaeenejad and M. Moghaddam, "Bistatic scattering from dielectric structures with two rough boundaries using the small perturbation method," IEEE Trans. Geosci. Remote Sens. **44**, 2102–2114 (2006).
5. Y. Altuncu, A. Yapar, and I. Akduman, "On the scattering of electromagnetic waves by bodies buried in a half-space with locally rough interface," IEEE Trans. Geosci. Remote Sens. **44**, 1435–1443 (2006).
6. D. E. Lawrence and K. Sarabandi, "Electromagnetic scattering from a dielectric cylinder buried beneath a slightly rough surface," IEEE Trans. Antennas Propag. **50**, 1368–1376 (2002).
7. A. Soubret, G. Berginc, and C. Bourrely, "Backscattering enhancement of an electromagnetic wave scattered by two-dimensional rough layers," J. Opt. Soc. Am. A **18**, 2778–2788 (2001).
8. I. M. Fuks and A. G. Voronovich, "Wave diffraction by rough interfaces in an arbitrary plane-layered medium," Waves Random Media **10**, 253–272 (2000).
9. Y. Zhang, Y. E. Yang, H. Braunisch, and J. A. Kong, "Electromagnetic wave interaction of conducting object with rough surface by hybrid SPM/MOM technique," Prog. Electromagn. Res. **22**, 315–335 (1999).
10. L. Tsang, J. A. Kong, K.-H. Ding, and C. O. Ao, *Scattering of Electromagnetics Waves: Numerical Simulations*, Series on Remote Sensing (Wiley, 2001).
11. P. J. Valle, F. Gonzalez, and F. Moreno, "Electromagnetic wave scattering from conducting cylindrical structures on flat substrates," Appl. Opt. **33**, 512–523 (1994).
12. P. J. Valle, F. Moreno, and J. M. Saiz, "Comparison of real- and perfect-conductor approaches for scattering by a cylinder on a flat substrate," J. Opt. Soc. Am. A **15**, 158–162 (1998).
13. A. Madrazo and M. Nieto-Vesperinas, "Scattering of electromagnetic waves from a cylinder in front of a conducting plane," J. Opt. Soc. Am. A **12**, 1298–1309 (1995).
14. A. Madrazo and M. Nieto-Vesperinas, "Scattering of light and other electromagnetic waves from a body buried beneath a highly rough random surface," J. Opt. Soc. Am. A **14**, 1859–1866 (1997).
15. X. Wang, C.-F. Wang, Y.-B. Gan, and L.-W. Li, "Electromagnetic scattering from a circular target above or below rough surface," Prog. Electromagn. Res. **40**, 207–227 (2003).
16. Chih-Hao Kuo and M. Moghaddam, "Electromagnetic scattering from a buried cylinder in layered media with rough interfaces," IEEE Trans. Antennas Propag. **54**, 2392–2401 (2006).
17. H. Ye and Y.-Q. Jin, "A hybrid analytic-numerical algorithm of scattering from an object above a rough surface," IEEE Trans. Geosci. Remote Sens. **45**, 1174–1180 (2007).
18. M. El-Shenawee, "Polarimetric scattering from two-layered two dimensional random rough surfaces with and without buried objects," IEEE Trans. Geosci. Remote Sens. **42**, 67–76 (2001).
19. M. El-Shenawee, C. Rappaport, and M. Silevitch, "Monte Carlo simulations of electromagnetic wave scattering from a random rough surface with three-dimensional penetrable buried object: mine detection application using the steepest-descent fast multipole method," J. Opt. Soc. Am. A **18**, 3077–3084 (2001).
20. J. T. Johnson and R. J. Burkholder, "A study of scattering from an object below a rough surface," IEEE Trans. Geosci. Remote Sens. **42**, 59–66 (2004).
21. L. Tsang, C. H. Chang, and H. Sangani, "A banded matrix iterative approach to Monte Carlo simulations of scattering of waves by large scale random rough surface problems: TM case," Electron. Lett. **29**, 1666–1667 (1993).
22. L. Tsang, C. H. Chang, H. Sangani, A. Ishimaru, and P. Phu, "A banded matrix iterative approach to Monte Carlo simulations of large scale random rough surface scattering: TE case," J. Electromagn. Waves Appl. **29**, 1185–1200 (1993).
23. D. Holliday, L. L. DeRaad Jr., and G. J. St-Cyr, "Forward-backward: a new method for computing low-grazing angle scattering," IEEE Trans. Antennas Propag. **44**, 1199–1206 (1995).
24. H. T. Chou and J. T. Johnson, "A novel acceleration algorithm for the computation of scattering from rough surfaces with the forward-backward method," Radio Sci. **33**, 1277–1287 (1998).
25. D. Torrungrueng, J. T. Johnson, and H. T. Chou, "Some issues related to the novel spectral acceleration method for the fast computation of radiation/scattering from one-dimensional extremely large scale quasi-planar structures," Radio Sci. **37**, 1–20 (2002).
26. N. Déchamps, N. De Beaucoudrey, C. Bourlier, and S. Toutain, "Fast numerical method for electromagnetic scattering by rough layered interfaces: Propagation-inside-layer expansion method," J. Opt. Soc. Am. A **23**, 359–369 (2006).
27. N. Déchamps and C. Bourlier, "Electromagnetic scattering from a rough layer: Propagation-inside-layer expansion method combined to an updated BMIA/CAG approach," IEEE Trans. Antennas Propag. **55**, 2790–2802 (2007).
28. N. Déchamps and C. Bourlier, "Electromagnetic scattering from a rough layer: propagation-inside-layer expansion method combined to the forward-backward novel spectral acceleration," IEEE Trans. Antennas Propag. **55**, 3576–3586 (2007).
29. Eric I. Thorsos, "The validity of the Kirchhoff approximation for rough surface scattering using a Gaussian roughness spectrum," J. Acoust. Soc. Am. **83**, 78–92 (1988).
30. A. Iodice, "Forward-backward method for scattering from dielectric rough surfaces," IEEE Trans. Antennas Propag. **50**, 901–911 (2002).
31. G. Kubické, C. Bourlier, and J. Saillard, "Scattering by an object above a randomly rough surface from a fast numerical method: extended PILE method combined to FB-SA," submitted to Waves Random Media 31 January 2008, TWRM-2008-007 (2008).